Energy Advances

ROYAL SOCIETY OF CHEMISTRY

PAPER

View Article Online
View Journal

Cite this: DOI: 10.1039/d5ya00312a

From synthesis to device: comparative study of Bi_2Te_3 alloys prepared by direct melt and ball milling for printed thermoelectrics

Swathi Krishna Subhash, *[ab] Stefano Morese,[ab] Uwe Pelz,[ab] Suman Kundu[ab] and Peter Woias[ab]

The synthesis route of thermoelectric (TE) materials strongly influences their microstructure and transport properties. However, few studies compare different synthesis processes of Bi_2Te_3-based alloys and their impact on the microstructure and thermoelectric properties of the resulting materials. Here, we compare n-type and p-type Bi_2Te_3-based alloys prepared *via* high-energy ball milling and direct melt processes. Ball milling is a simpler, low-cost, room-temperature process that eliminates the need for high-temperature furnaces. The direct melting method used here closely resembles commercial melting techniques for polycrystalline materials. In this study, both routes yielded TE materials with similar crystallinity, morphology, and phase purity. The powders obtained were then converted into binder-free printable inks. At 300 K, the measured ZT ranged from 0.1 to 0.5, limited by low electrical conductivity, while a high Seebeck coefficient and low thermal conductivity (0.2–0.3 W m^{-1} K^{-1}) were achieved. Energy consumption analysis indicates that ball milling requires 3–5 times less energy per gram than melt synthesis. Planar thermoelectric generators (PTEGs) were fabricated on a polyimide substrate by a simple four-step process, using the inks derived from both synthesis routes. The milled-material PTEG exhibited an open-circuit voltage of 86.7 mV at ΔT = 40 K and delivered a higher power output than the melt-material device, due to the lower electrical resistance achieved at the device level. This work demonstrates that high-energy ball milling provides a scalable and energy-efficient route to printable thermoelectric materials, enabling low-grade temperature energy harvesting applications.

Received 28th October 2025,
Accepted 28th March 2026

DOI: 10.1039/d5ya00312a

rsc.li/energy-advances

Introduction

The increasing global demand for energy and growing environmental concerns have encouraged intensive research into sustainable energy solutions. Thermoelectric (TE) materials are promising energy conversion materials that can directly convert thermal energy into electrical energy *via* the Seebeck effect. This phenomenon originates from the coupling of charge and heat transport in materials and has proven particularly useful for power generation and TE-based cooling. The performance of a TE material is defined by the thermoelectric figure of merit $ZT = S^2\sigma T/\kappa$, where S, σ, κ and T are the Seebeck coefficient, the electrical conductivity, the thermal conductivity (κ, the sum of phonon κ_l and electronic κ_e components), and the absolute temperature, respectively. Achieving a high ZT requires a large Seebeck coefficient, high electrical conductivity and low thermal conductivity. However, these transport characteristics are interdependent through material properties like carrier concentration and carrier mobility.[1] Thus, the optimization of ZT requires trade-offs.

Over the past decades, a wide range of TE materials with remarkable ZT values, like Bi_2Te_3,[2] GeTe,[3] $AgSbTe_2$,[4,5] Skutterudites,[6,7] half-Heusler[8,9] and PbSe,[10] have been introduced. Bismuth telluride (Bi_2Te_3) and its alloys ($Bi_{2-x}Sb_xSe_yTe_{3-y}$) are the most favoured materials for commercial applications owing to their remarkable TE properties near room temperature.[11]

A wide range of synthesis routes have been employed to produce Bi_2Te_3-based thermoelectric materials. Among them are unidirectional solidification methods like zone melting (ZM), which is a mainstream commercial fabrication technique, yielding high-purity and highly crystalline materials.[12,13] In this process, a narrow molten region is slowly passed through the material, which allows the impurities to segregate in the molten zone, leaving behind a pure homogeneous crystal. Directional solidification in ZM promotes crystallographic orientation, leading to strong anisotropic electric properties.[14] However, ZM is an energy-intensive, time-consuming, and

[a] Department of Microsystems Engineering – IMTEK, University of Freiburg, Germany. E-mail: swathi.subhash@imtek.uni-freiburg.de
[b] Cluster of Excellence livMatS@FIT – Freiburg Center for Interactive Materials and Bioinspired Technologies, University of Freiburg, Germany

equipment-dependent process, requiring sophisticated temperature control systems. Moreover, their solid bulk form makes them difficult to process as thermoelectric inks, which are often needed for printing or customizable electronics. To address this, ZM ingots must be milled into powders, adding an extra fabrication step. Although this technique is reported to produce high-quality materials, its reliance on multiple processing stages increases complexity, energy consumption, and overall processing time.

In contrast, high-energy ball milling offers a scalable and cost-effective route to tailor the microstructure and transport properties of thermoelectric materials, particularly in Bi_2Te_3-based systems.[15] In this process, the elemental precursors are mechanically alloyed into a fine powder in a single step. This technique is advantageous for TE materials, as intense mechanical impacts produce nanoscale powders with a high density of grain boundaries.[16] When consolidated, these dense interfaces are beneficial in scattering phonons more effectively than charge carriers, thereby reducing the lattice thermal conductivity without severely compromising electrical transport.[17] Studies on Bi_2Te_3 milled for controlled durations show that optimizing milling time generally decreases thermal conductivity, while often increasing carrier concentration and electrical conductivity, leading to an improved power factor and figure-of-merit (*ZT*) after subsequent consolidation by spark plasma sintering or hot pressing.[18–20] For example, Pundir *et al.* demonstrated that optimizing the ball milling time to 8 hours for Bi_2Te_3, powders followed by spark plasma sintering, minimized the crystallite size and maximized phonon scattering, yielding a peak *ZT* value of 1.22 at 473 K.[16] Similarly, Son *et al.* achieved a high *ZT* of 1.14 at 323 K in p-type $(Bi,Sb)_2Te_3$ by carefully tailoring the milling duration to 10 hours.[17] Systematic investigations demonstrate that optimization of milling parameters, like milling time and rotational speed, play crucial roles in tuning the delicate balance between the Seebeck coefficient, electrical resistivity, and thermal transport.[21,22] These trends make mechanical milling a highly compelling and scalable strategy for engineering high-performance Bi_2Te_3 thermoelectric alloys near room temperature.

However, despite the progress in synthesis techniques, a systematic comparison between ball milling and conventional routes, particularly in terms of their thermoelectric properties and energy costs associated with the process, remains lacking. Most existing research focuses either on optimizing individual synthesis strategies or on post-processing methods like spark plasma sintering (SPS),[23,24] which remains incompatible with flexible, large-area, or low-temperature fabrication requirements. This lack of direct comparison limits our understanding of how synthesis pathways influence material properties and scalability. Addressing this gap is essential for identifying synthesis routes that can deliver high-performance, energy-efficient, and commercially viable thermoelectric materials.

Beyond material synthesis, the development of scalable and low-cost device fabrication techniques is critical for next-generation thermoelectric devices. A recent trend in the fabrication of thermoelectric generators (TEGs) suitable for flexible electronics is the use of printing techniques, such as inkjet,[25,26] direct writing,[27] screen printing[28,29] and dispenser printing.[30,31] These approaches eliminate the need for expensive processing steps, such as lithography, or physical and chemical vapor deposition and etching. Among them, dispenser printing is a cost-effective and user-friendly method that does not necessitate high-temperature curing.

In this work, we systematically compare two fundamentally distinct synthesis approaches for both n-type and p-type Bi_2Te_3 alloys: high-energy ball milling and direct melt synthesis. Unlike zone melting (ZM), which passes a molten zone gradually through the ingot, direct melt synthesis involves melting the entire batch in a single step, followed by solidification. To enable a fair comparison in powder and ink forms, the bulk ingot from the direct melt is briefly ball-milled (30 min) to make it suitable for ink formulation. Thermoelectric inks produced from both methods are prepared and compared. This comparison allows us to study the influence of the synthesis route on crystallinity, phase purity, microstructure, and thermoelectric performance. Our results show that both routes produce powders with similar microstructural and thermoelectric characteristics. Building upon the trend for printable TEGs, we further demonstrate the fabrication of a planar TEG (PTEG) on a polyimide substrate. A four-step fabrication of printed PTEGs using pristine powder-based inks, without polymer binders, is presented. This combined synthesis-device workflow highlights a practical and scalable pathway for advancing next-generation flexible thermoelectric platforms.

Methodology

Materials

Bismuth (99.999%), tellurium (99.999%), antimony (99.999%), selenium (99.999%) and terpineol (90%, technical grade) were purchased from Sigma-Aldrich/Merck (Darmstadt, Germany).

Synthesis of thermoelectric materials and thermoelectric ink

Two synthesis routes were investigated: high-energy ball milling and direct melt processes. For ball milling, Bi, Te, and Sb (p-type) or Se (n-type) were weighed according to the stoichiometric ratios of $Bi_{0.5}Sb_{1.5}Te_3$ and $Bi_2Te_{2.7}Se_{0.3}$. The elements were loaded into a water-cooled 50 mL stainless steel jar along with 10 steel balls, of 10 mm diameter, each weighing approximately 4 g. The ball-to-powder ratio was maintained at 5 : 1. High-energy ball milling (Emax, Retsch, Germany) was carried out for 4.5 h at 1000 rpm, with 1 min interruptions every 10 min to prevent overheating. The milling direction was reversed periodically to ensure homogeneous alloying. The resulting powder was sieved (Sieve Shaker AS 200 Control, Retsch, Germany) using 100 μm and 50 μm meshes to obtain the final product.

For the direct melt process, the elements were weighed according to the same stoichiometry and sealed in evacuated quartz ampoules. The sealed ampoules were heated at 700 °C for 13 h for the p-type and 3 h for the n-type. Sb has the highest

melting point (630 °C) and larger atomic radius, so Sb-rich alloys require longer heating for homogeneous mixing, while n-type Se is low-melting and volatile, so prolonged heating can lead to loss of Se. Once the elements had melted, the samples were quenched in liquid nitrogen. The resulting ingots were mechanically fractured and subjected to 30 min of ball milling at 1000 rpm. This brief milling was sufficient to reduce the particle size for sieving (120 μm and 50 μm meshes) without altering the composition or inducing additional alloying, in contrast to the longer mechanical alloying step. The powders were then sieved in 120 μm and 50 μm meshes as before.

The thermoelectric inks were prepared by mixing TE powder with a terpineol solvent without any additional binder. Inks with 88 wt% (p-type) and 80 wt% (n-type) powder loading were created using a vortex mixer (IKA orbital shaker, Vortex 2).

Characterization

The phase composition and purity of the powders were analysed with a STADI P powder diffractometer (STOE & Cie GmbH, Germany) equipped with Mo-K-alpha-1 radiation. The powder samples were used to fill 0.7 mm diameter quartz capillaries inside a glove box to prevent exposure to air and moisture. The open ends of the capillaries were flame-sealed. Measurements were performed in Debye–Scherrer geometry over a 2θ range of 10–80° with a step size of 0.01° and a scan speed of 0.1° min^{-1}. The data was processed with the STOE WinX POW software package.

Microstructural analysis and elemental composition, including elemental mapping, were performed using a field emission scanning electron microscope (FE-SEM) integrated with an energy-dispersive spectrometer (EDS) (FEI Scios 2 HiVac system Thermo Fischer, USA). Powder samples were mounted on SEM stubs using double-sided conductive carbon tape, and gently tapped to ensure even distribution.

For the thermoelectric property measurement, the inks were first deposited onto an FR4 substrate and dried at 50 °C on a hotplate. The coated substrates were then subjected to stepwise hot pressing from 100 °C to 180 °C in 25 °C increments with a 10 min dwell at each temperature, to densify the films and remove residual solvent.

The Seebeck coefficient was determined using a custom-built measurement platform. During the measurement, a temperature gradient was applied across the sample using two independently temperature-controlled aluminium stages. The resulting voltage was recorded simultaneously along with the sample temperature. The electrical measurements are conducted on a Keithley 3706 System Switch/Multimeter. The Seebeck coefficient of the sample was calculated from the measured temperature difference and thermoelectric voltage, accounting for the known Seebeck coefficients of the measurement leads. Further details of the measurement concept and setup are provided in the SI (Fig. S1).

Electrical conductivity was determined by the four-point/van der Pauw method. A schematic of the measurement setup is shown in Fig. S2. During the measurement, four small contacts are placed on the sample perimeter, current is passed through two contacts, and the voltage is measured across the other two. Thermal conductivity was measured using a transient hot bridge (THB) system (THB 100, Linseis Messgeräte GmbH, Germany) equipped with a hot point sensor. For this purpose, TE material blocks of size 5 × 5 mm^2 were prepared. The hot point sensor was positioned between two halves of the sample, and a constant heating current was applied to the sensor, resulting in localized heating of the surrounding material. The temperature rise as a function of time was used to determine the thermal conductivity of the thermoelectric samples. A detailed description of the measurement principle and additional schematics are provided in SI Fig. S3. All thermoelectric properties were measured on three independently prepared samples on the FR4 substrate for each material composition.

Planar TEG (PTEG) fabrication and characterization

The fabrication process of the TEG and a representative image of a prepared TEG are shown in Fig. 1. Devices were fabricated on a polyimide substrate, coated on one side with a 30 μm copper layer, serving as an electrode. The fabrication process involved four main steps: (i) contact structuring, (ii) application of a laser-patterned Kapton mask, (iii) deposition of thermoelectric (TE) inks, and (iv) hot pressing.

In the first step, the electrical contacts were patterned on the copper layer *via* laser ablation (LPKF ProtoLaser U4). The substrate was then cleaned with a 1 M HCl solution to remove surface oxides, followed by light mechanical abrasion to increase surface roughness and improve adhesion. In the second step, a laser-structured Kapton tape was applied onto the substrate to prevent mixing of p-type and n-type inks during deposition.

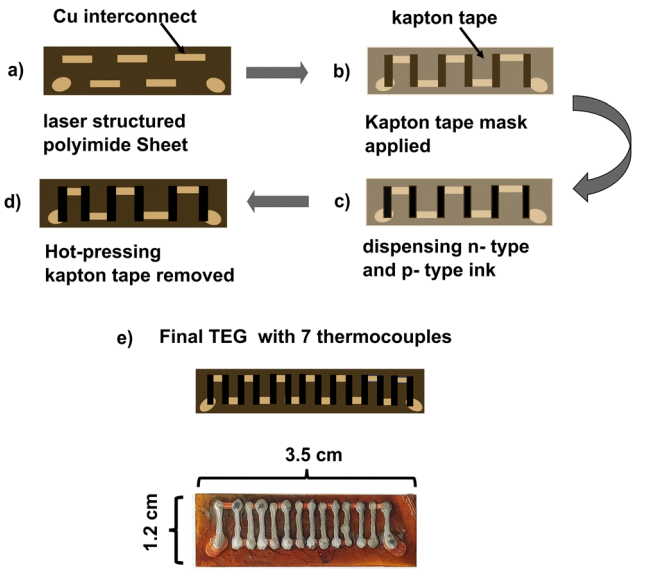

Fig. 1 Process flow of TEG fabrication: (a) laser structuring of the polyimide sheet to form the copper interconnect between legs, (b) applying laser-structured Kapton tape as a mask to avoid mixing of p- and n-type ink, (c) dispensing of thermoelectric ink, (d) hot-pressing and removal of the Kapton mask, (e) image of the final TEG with 7 thermocouples.

In the third step, TE inks were dispensed using a digital dispenser (DX350, Oki Electric Industry Co., Ltd, Japan) at approximately 1.5 bar. Finally, the deposited legs were consolidated by hot pressing under the same conditions described in section 'Characterization', after which the Kapton mask was mechanically removed.

The final TEG had lateral dimensions of 3.5 cm × 1.2 cm and contained 14 thermocouples in series. The individual leg dimensions were approximately 1 mm × 7 mm. The electrical resistance and open-circuit voltage of the TEG were measured using a digital multimeter, while temperature gradients were applied using the custom-built Seebeck measurement platform. During testing, TEGs were placed between a hot plate and a cold plate to establish a controlled temperature difference. The corresponding illustration of the planar TEG performance measurement setup is shown in Fig. S3.

Results and discussion

Structure, morphology and composition

The phase composition of the as-prepared $Bi_{0.5}Sb_{1.5}Te_3$ (p-type) and $Bi_2Te_{2.7}Se_{0.3}$ (n-type) powders obtained from ball milling and direct melt, characterized by powder XRD, is presented in Fig. 2. For the p-type material, all the XRD peaks match the standard JCPDS card 49-1713 for $Bi_{0.5}Sb_{1.5}Te_3$. For the n-type melt sample, the pattern matches well with 51-0643 for $Bi_2Te_{2.7}Se_{0.3}$, while the milled sample shows slight peak shifts and reduced intensity near 45°. This is likely due to some microstrains from the longer milling process. Both TE materials crystallized in a single-phase rhombohedral crystal structure (space group $R\bar{3}m$). No secondary phases were observed in the XRD.

The average crystallite size estimated using the integral breadth method was approximately 16 nm for p-type and 14 nm for n-type powders, independent of the synthesis route. This demonstrates that both ball milling and direct melt plus short-duration milling produced comparable microstructural refinement, without additional coarsening or size reduction. No preferred (00l) orientation was observed in either composition. However, in the p-type samples, a slight change in the relative intensity for the (1010) and (110) planes was observed in both samples. In the standard JCPDS pattern, the (1010) plane exhibits higher intensity than the (110) plane. In both the melt and milled samples, the (1010) peak intensity is reduced while the (110) peak is relatively enhanced, indicating a shift in preferred orientation or partial loss of crystallinity for specific planes. Overall, these results indicate that both synthesis routes reliably produce phase-pure rhombohedral Bi_2Te_3-based alloys with similar crystallite sizes and subtle textural variations.

The morphological features obtained by SEM for the as-prepared powder samples are shown in Fig. 3, along with their EDS spectra. For the ball-milled samples, the powder consisted primarily of fine particles in the submicron range (<1 μm) with rough surfaces. However, large agglomerates of size 10–50 μm were also observed, likely due to particle clustering during

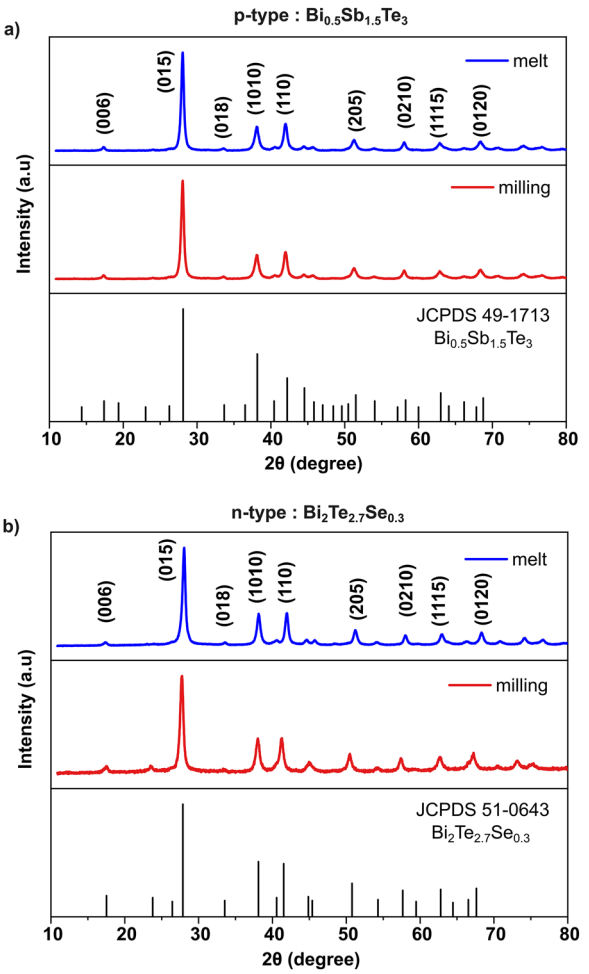

Fig. 2 The room-temperature powder X-ray diffraction of (a) p-type material (melt and milled samples along with JCPDS 49-1713) and (b) n-type material (melt and milled samples along with JCPDS 51-0643).

milling. Direct melt-processed ingots, subjected to short-duration milling (30 min), exhibited a similar microstructure, with comparable particle size distribution and surface roughness.

These observations indicate that even brief milling of the melt-processed ingots produces a particle morphology similar to that obtained from extended high-energy ball milling. This similarity in microstructural features suggests that powders from both synthesis routes are likely to exhibit comparable mechanical and thermoelectric behaviour.

The distribution of the elements in the prepared samples was analysed using SEM-EDS elemental mapping. As can be seen in Fig. 4(a–d) all the elements are accordingly uniformly distributed throughout all the p-type and n-type samples. It also confirms that there is no single elemental segregation in the sample, showing proper alloying of elements into p-type and n-type materials. The chemical composition of the samples determined by EDS is shown in the tables along with the mapping results in Fig. 4. The obtained values show that all the samples have near stoichiometric and homogeneous composition.

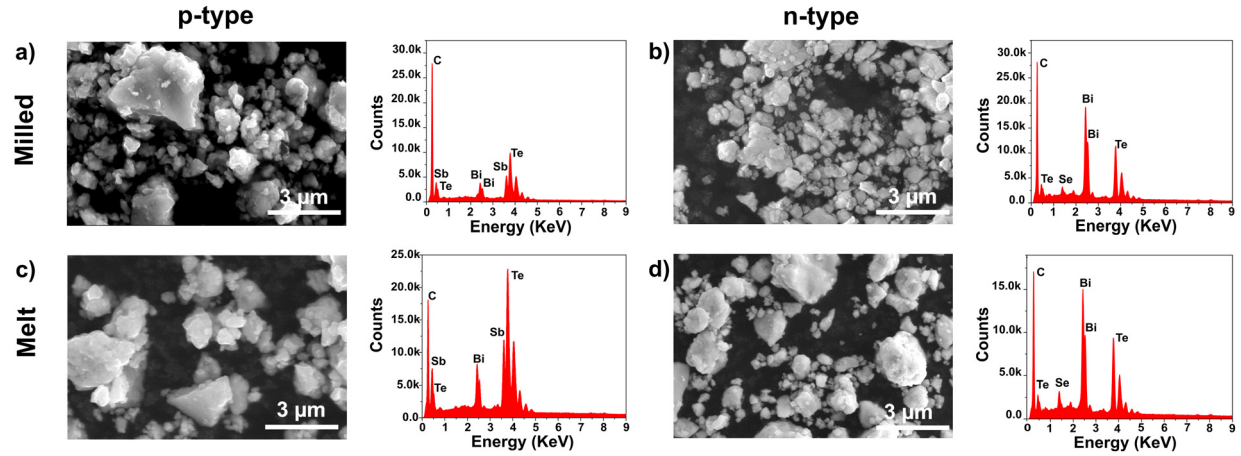

Fig. 3 SEM images of the powder samples showing the surface morphology along with the obtained EDS spectra confirming the elements present in each sample: (a) milled p-type, (b) milled n-type, (c) melt p-type, (d) melt n-type.

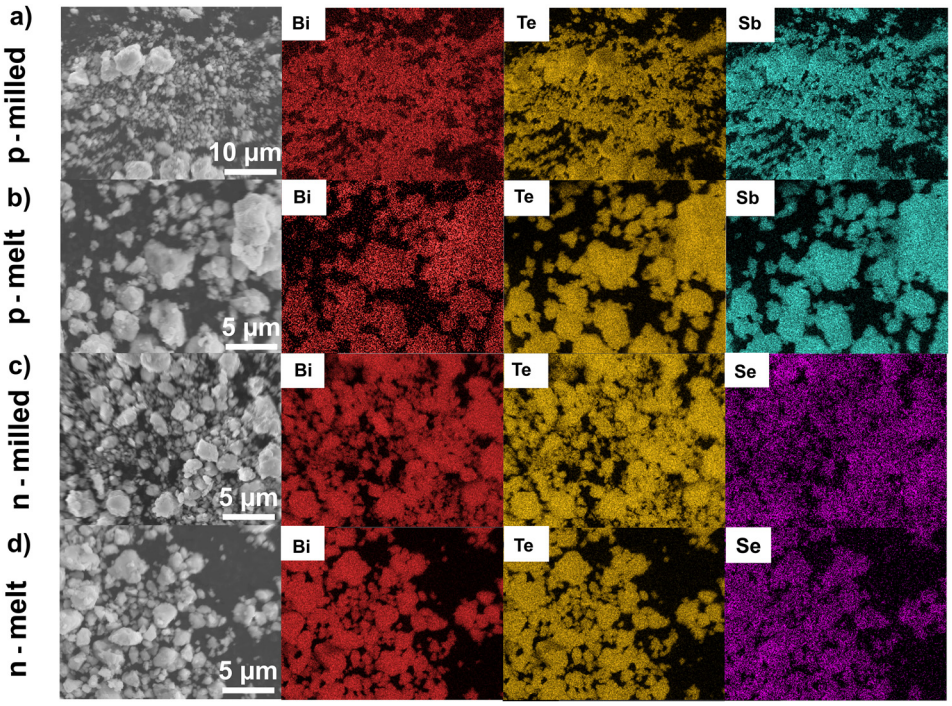

Elements	Norm. atom%
Bi	38.4
Te	54.8
Se	6.4

Elements	Norm. atom%
Bi	37.6
Te	53.2
Se	9.1

Elements	Norm. atom%
Bi	9.8
Te	60.8
Sb	29.4

Elements	Norm. atom%
Bi	9.3
Te	60.9
Sb	29.8

Fig. 4 EDS elemental mapping of the samples, with the weight percentage presented in the tables: (a) milled p-type, (b) melt p-type, (c) milled n-type, (d) melt n-type.

High-energy ball milling using a stainless steel jar and balls results in a high chance of introducing iron (Fe) wear and contamination due to wear of the milling media, particularly with prolonged milling duration.[22,32] In this study, the milled powders were analysed using EDS (elemental mapping) and XRD for possible traces of Fe. However, no measurable Fe signal was observed in the EDS analysis within the detection limits of the technique (0.08–0.1 wt%),[33] and no Fe-containing secondary phases were detected in the XRD patterns. While there may be some iron contamination, the lack of secondary phases and consistent thermoelectric properties suggest it is minimal.

The reduction of iron wear in this study is attributed to the optimized high-energy milling parameters. While mechanical alloying of bismuth telluride systems often utilizes extended durations ranging from 4 to 48 hours,[15,17,34] the high rotational speed (1000 rpm) applied in this work allowed for complete alloying within a short time of 4.5 hours. Dasgupta *et al.* demonstrated that lower milling speeds requiring longer duration significantly increase Fe contamination, reporting an increase from ~1.5 wt% Fe at 500 rpm (3 h) to ~4 wt% Fe after milling at 350 rpm (14 h).[35] More specifically for bismuth-telluride-based alloys, Son *et al.* quantified iron wear using ICP

analysis and showed that Fe contamination remains negligible (<0.01 wt%) for milling times up to 5 h, whereas prolonged milling durations of 10–48 h led to substantial Fe accumulation (0.08–0.67 wt%).[17] Thus, the short 4.5 h duration used in this study places the process well within a low-contamination regime and effectively mitigates iron wear from the milling media.

Thermoelectric properties of the material

The electrical conductivities of both p-type and n-type materials for milled and melt samples are summarized in Table 1. For the n-type material, the average conductivities were 60.6 S cm^{-1} for the milled samples and 98.6 S cm^{-1} for the melt samples. For the p-type material, the corresponding values were 54.3 S cm^{-1} (milled) and 57.3 S cm^{-1} (melt). These values are notably lower than that for typical bulk polycrystalline ($\sim$600–1000 S cm^{-1}), but still indicate that the powders are conductive rather than insulating.

For the n-type material, the melt sample exhibited higher electrical conductivity than the milled counterpart. EDS analysis revealed a slightly higher Se content in the melt n-type sample compared with the nominal stoichiometry. According to the literature, with increasing Se content, the electrical conductivity decreases due to reduced carrier mobility.[36] In the present case, however, the combined effects of carrier concentration and microstructure appear to outweigh the adverse effect of higher Se content.

Interestingly, the p-type samples resulted in similar electrical conductivity irrespective of their synthesis routes. XRD analysis confirmed the absence of secondary phases. SEM showed that both have very similar microstructures, and EDS data show that the composition is close to the expected stochiometric ratio. Thus, the most likely reason for the reduced conductivity is microstructural factors. A highly porous sample (low-density sample), amorphous or disordered intergranular regions and point defects are the most plausible microstructural defects causing reduced electrical performance. Low density, in particular, can result in poor grain-to-grain contact and numerous micro/nanopores disrupting the electrical paths. These structural defects hinder the effective percolation pathways for both electrons and phonons, resulting in diminished electrical and thermal conductivity.[37]

The mean Seebeck coefficient values of n-milled and n-melt are −187.17 μV K^{-1} and −181.37 μV K^{-1}, respectively. These values are slightly higher than the near-room-temperature values of −160 to −170 μV K^{-1} reported in the literature for $Bi_2Te_{2.7}Se_{0.3}$.[10,38] For the p-milled and p-melt samples, the mean values were 146.80 μV K^{-1} and 101.8 μV K^{-1}, respectively, which are lower than the reported literature values of around 200 μV K^{-1}.[39] The small differences between the melt and milled samples are likely due to the variations in carrier concentration and microstructural differences. As expected from theory, the magnitude of the Seebeck coefficient is inversely related to carrier concentration and electrical conductivity. Thus, the previously reported low electrical conductivity values combined with a reasonably high Seebeck coefficient are consistent with this inverse relationship—lower carrier concentration increases the Seebeck coefficient but reduces electrical conductivity.

Thermal conductivity measured for all the samples was in the range 0.20–0.34 W m^{-1} K^{-1} for a thickness of 1.1–1.2 mm (Table 1). These values are significantly lower than the typical bulk values. Which range between 1 and 2 W m^{-1} K^{-1}. Highly engineered or nanostructured samples have achieved reduced lattice thermal conductivity and overall thermal conductivity values around or slightly below 0.4–0.5 W m^{-1} K^{-1}, approaching the theoretical limits for dense bulk samples.[11]

The exceptionally low thermal conductivity observed in the present samples aligns with our prior findings (low electrical conductivity), indicating highly porous samples, with micro/nanosized pores, thus reducing phonon transport. The reduction in thermal conductivity is consistent with the simultaneously observed low electrical conductivity, reflecting poor grain-to-grain contact and structural defects that disrupt both electron and phonon percolation pathways.

The *ZT* values at 300 K calculated from the measured Seebeck coefficient, electrical conductivity, and thermal conductivity ranged from 0.1 to 0.5. The overall *ZT* obtained is not as high as the state-of-the-art value presented in the literature (0.5–1). Despite showing reasonable Seebeck coefficient values and extremely low thermal conductivity, the *ZT* is low because of the extremely low electric conductivity. Even though the *ZT* is low; it is reasonable for poorly densified samples with low σ and κ—especially those with suboptimal electrical conductivity, but extremely low thermal conductivity, as for our samples.

From the aforementioned results, it is interesting to note that the thermoelectric properties of the materials are similar, irrespective of their synthesis routes. This can be attributed to the similar microstructure developed throughout the complete processing route: ball-milling, melt-processing samples and final ball milling of the melt-processed samples. The presence of smaller submicron particles introduces additional grain boundaries and interfaces, which effectively scatter long-wave phonons. This, combined with the likely low density of the sample, explains the observed low thermal conductivity and comes at the expense of the electrical properties. To further

Table 1 Thermoelectric properties measured for the materials from the milling and melt synthesis with the standard deviation

	p-milled	p-melt	n-milled	n-melt
Electrical conductivity (S cm^{-1})	54.3 ± 7.3	57.3 ± 12.6	60.6 ± 5.7	98.6 ± 12.8
Seebeck coefficient (μV K^{-1})	146.8 ± 1.2	101.1 ± 2.4	−187.2 ± 10.2	−181.4 ± 3.8
Thermal conductivity (W m^{-1} K^{-1})	0.34 ± 0.02	0.22 ± 0.01	0.27 ± 0.01	0.21 ± 0.01
ZT	0.1	0.1	0.3	0.5

enhance the electrical performance, while maintaining low thermal conductivity, requires improved densification of the samples. This could reduce the porosity and increase the grain-to-grain connectivity for better carrier mobility. Microstructural control is equally important: while fine grains and a larger total interfacial area reduce the lattice thermal conductivity, highly defective grain boundaries can reduce the carrier mobility. Therefore, optimizing the ball milling parameters along with the hot-pressing process could help to tune the material properties and achieve a better balance between electrical and thermal conductivity.

Consequently, the thermoelectric performance of these materials could be further improved by increasing the electrical conductivity (σ) while retaining the advantage of reduced thermal conductivity (κ). Such optimization would maximize the figure of merit (ZT) without sacrificing the benefits of the low-thermal-conductivity microstructure.

Energy consumption estimation

The approximate electrical energy consumption of ball milling and melt synthesis can be compared for the batches prepared in this work. For ball milling, the energy consumption was calculated based on the rated power (available from the manufacturer) and the milling time. For the melt synthesis, the major energy contribution comes from the furnace melting step, and the energy was calculated using the heating time and the average furnace power.

The calculated energy consumption per gram of material was estimated as 1575 kJ g^{-1} for ball milling (32 g batch, n- and p-type), 5738 kJ g^{-1} for melt synthesis for n-type (16 g batch), and 8438 kJ g^{-1} for melt synthesis for p-type (16 g batch). This comparison shows that ball milling requires 3–5 times less energy per gram than melt synthesis, primarily because the prolonged ramping and holding stages dominate the energy demand of the direct melt process.

Both methods are scalable, but in different ways. Ball milling can be scaled by using a bigger jar while maintaining the ball-to-powder ratio. Conversely, melt synthesis can accommodate multiple ampoules per furnace run to lower the effective energy per gram. Nevertheless, ball milling offers the advantage of single-step powder production, with minimal manual work and without demanding complex operational setups.

Performance of planar TEG

To demonstrate the feasibility of printing planar TEGs using the thermoelectric ink derived from the two synthesis routes, two prototype devices were fabricated. Planar TEG 1 (PTEG1) was fabricated from n-type and p-type ink obtained from ball milling and planar TEG 2 (PTEG2) was fabricated from inks obtained by the melt process. The measured device resistance was 777.7 Ω for PTEG1 and 2.4 kΩ for PTEG2. The corresponding images are shown in Fig. S4(a and b).

When a temperature difference (ΔT) was applied across the devices, a corresponding open-circuit voltage (V_{oc}) was generated. The V_{oc} *vs.* ΔT plots obtained for both devices are also presented in Fig. 5(a). V_{oc} varied approximately linearly with ΔT,

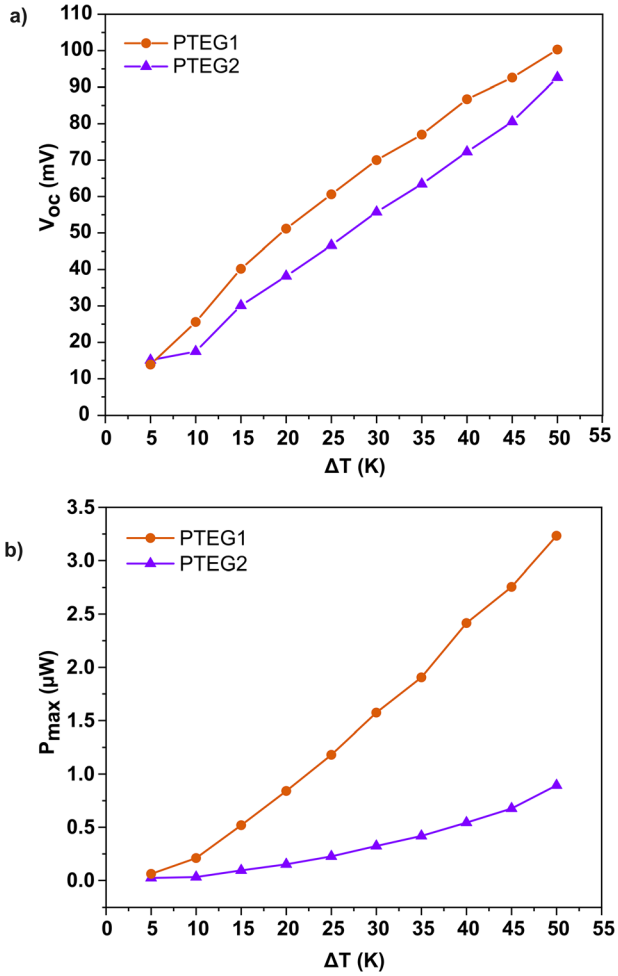

Fig. 5 Performance of TEGs: (a) V_{oc} *vs.* ΔT plot obtained for both PTEG devices, (b) P_{max} *vs.* ΔT plot obtained for both PTEG devices.

allowing the Seebeck coefficient (S) to be calculated from the slope of the linear fit, according to the equation:

$$S = \frac{V_{oc}}{\Delta T}$$

The calculated Seebeck coefficients for the pair (Sp–Sn) are 280 μV K^{-1} and 248 μV K^{-1} for the milled and melt samples, respectively. These values are slightly lower than those measured for the intrinsic pair (measured after ink formulation), which are 334 μV K^{-1} for the milled and 283 μV K^{-1} for the melt samples. The lower calculated values may result from thermal losses to the surrounding air or overestimation of the applied ΔT across the TEG. The maximum power can be calculated using the equation:

$$P_{max} = \frac{V_{oc}^2}{4R_i}$$

where R_i is the internal resistance. For PTEG1, at ΔT of 30 K, 40 K, 50 K, the calculated P_{max} are 1.6, 2.4, and 3.2 μW, respectively. For PTEG2, due to its higher electrical resistance, the P_{max} values are reduced to 0.3, 0.5, 0.9 μW at the same ΔT

Table 2 Power performance of printed planar TE materials compared to the literature

Material	Binder	Process	Device dimension	TE legs	R_{in}	V_{oc}	P_{max}
[40]rGO/Bi_2Te_3	PVP	Write	10 mm × 3 mm × 40 mm	6	7.8 Ω calculated	15.3 mV@40 K	7.48 μW@40 K
[30]Bi_2Te_3/1 wt % of Se	Epoxy and hardener	Dispenser	5 mm × 700 μm × 120 μm	62	480 Ω	220 mV@20 K	25 μW@20 K
[29]$Bi_{1.8}Te_{3.2}/Sb_2Te_3$	Epoxy	Screen	20 mm × 2 mm	8	592 Ω	32 mV@20 K	0.44 μW@20 K
[41]$Bi_{0.5}Sb_{1.5}Te_3/Bi_2Te_3$	PVP	Dispenser	length: 10 mm, diameter: 800 μm	10	37.9 Ω calculated	59.2 mV@60.8 K	23.97 mW@60.8 K
[25]$Bi_2Te_3/Bi_{0.5}Sb_{1.5}Te_3$		Inkjet		10	3.9 kΩ	46 mV@32.5 K	0.13 nW@32.5 K
[42]$Bi_{0.55}Sb_{1.45}Te_3$		FDM	2 mm × 25 mm	20	6.7 kΩ	70.7 mV@21 K	0.24 μW@21 K
[31]$Bi_{0.4}Sb_{1.6}Te_3/Bi_2Se_{0.3}Te_{2.7}$		Dispenser	10 mm × 1.5 mm	20	140 Ω	76.9 mV@30 K	8.4 μW@30 K
$Bi_{0.5}Sb_{1.5}Te_3/Bi_2Se_{0.3}Te_{2.7}$		Dispenser	1 mm × 7 mm	14	778 Ω	86.7 mV@40 K	2.4 μW@40 K
PTEG1							

values. At ΔT = 40 K, the measured V_{oc} values were 86.7 mV for PTEG1 and 71.1 mV for PTEG2, as shown in Fig. S4(c and d).

The prototype developed in this work currently exhibits less than ideal electrical resistance. This is primarily due to the electrical contact resistance between the printed legs and the Cu interconnects. The poor wettability of the thermoelectric ink on copper likely arises from surface energy mismatch between the solvent medium and the metallic substrate, leading to weak adhesion. Introducing an interfacial Ni layer could enhance surface compatibility and act as a diffusion barrier, improving both adhesion and electrical contact quality. Although the Cu surface was mechanically roughened and treated with HCl to remove oxides before dispensing the ink, the contacts still showed poor adhesion and high contact resistance. Furthermore, the inherent brittleness of the thermoelectric material led to minor cracks along the printed TEG legs, which further increased the overall resistance.

The fabricated planar TEG showed a similar trend in the V_{oc} *vs.* ΔT plot. However, the PTEG1 fabricated from the milled materials showed slightly higher V_{oc} output, which can be attributed to the higher Seebeck coefficient of the milled materials. In terms of maximum output power, PTEG2 exhibited a value approximately 79% lower than that of PTEG1, due to its higher contact resistance. It should be emphasized that this large difference in total resistance between the two devices arises from fabrication-induced variations in contact adhesion and micro-cracking, rather than differences in the intrinsic conductivities of the synthesized powders. The device resistance could be further reduced through surface modifications, such as increasing the surface roughness by laser-induced microstructures on the copper interconnects.

The TEG developed in this work shows the feasibility of a two-step fabrication process for planar TEGs using laser microstructuring and dispenser printing technology. This process also removes additional solvents from the thermoelectric ink and is compatible with low-temperature substrates. It is important to highlight that the thermoelectric ink used in this work consists of pristine materials post-synthesis, without any binders or polymer additives. In their current state, the TEGs have not been optimized for a specific application. However, with improvements in material properties and device resistance, the TEGs could be suitable for low-grade temperature applications, especially as a viable energy harvesting source for low-power sensors or IoT devices.

Table 2 compares the performance of the planar TEGs developed in this work with those of previously reported printed planar devices. The resistances of the devices fabricated in this work are comparable to those reported for devices without binders. The values of V_{oc} and P_{max} are comparable, and in some cases, they even exceed the reported values. With further optimization to reduce resistance, higher power output could be achieved. Considering the simplicity of fabrication, use of pristine materials, and compatibility with low-temperature substrates, these results demonstrate the feasibility of the proposed approach and its potential for low-grade temperature energy harvesting.

Conclusions

This study presents a comparative investigation of two scalable synthesis routes for Bi_2Te_3-based thermoelectric alloys: high-energy ball milling and direct melt processes. Both p-type and n-type alloys were synthesized and converted into printable thermoelectric ink without any additives or binders. The inks were characterized after low-temperature hot pressing, and their feasibility for the fabrication of planar TEGs was demonstrated through simple four-step TEG fabrication.

Both synthesis routes resulted in similar crystallinity and microstructure for the TE materials. However, the thermoelectric properties of the materials varied slightly from one another. Moderate Seebeck coefficients combined with ultra-low thermal conductivity ($\sim$0.2–0.3 W m^{-1} K^{-1}) were achieved. However, relatively low electrical conductivity ($<$100 S cm^{-1}) resulted in the overall ZT ranging from 0.1 to 0.5. These values are low but reasonable, considering the likely poorly densified and unoptimized nature of the synthesized samples.

To demonstrate the potential of binder-free thermoelectric inks, which are less common in the literature, a planar TEG was fabricated using inks derived from both milled and melt materials. Both devices exhibited linear Seebeck voltage response to applied temperature gradients, with the milled-material device (PTEG1) outperforming the melt-material device (PTEG2) due to a higher Seebeck coefficient and a lower

internal resistance. Although the output power remained limited by high internal resistance and poor electrical contacts, this proof-of-concept demonstrates the feasibility of a simplified, four-step printed TEG fabrication workflow using pristine thermoelectric powders.

Overall, the findings and analysis of energy consumption show that high-energy ball milling is a commercially viable alternative to melting-based methods. It provides a scalable and energy-efficient route to printable thermoelectric materials. These materials are suitable for low-grade temperature energy harvesting applications.

Conflicts of interest

There are no conflicts to declare.

Data availability

The data supporting this article have been included in the article and in the supplementary information (SI) and will be made available upon considerable request. Supplementary information is available. See DOI: https://doi.org/10.1039/d5ya00312a.

Acknowledgements

This work has been funded by the Deutsche Forschungsgemeinschaft (DFG, German Research Foundation) under Germany's Excellence Strategy – EXC-2193/1 – 390951807. The authors gratefully acknowledge Dr Thilo Ludwig and Dr Michael Daub from the Institute for Inorganic and Analytical Chemistry, University of Freiburg, for their guidance during the synthesis process and for assistance with XRD measurements. We also thank Ms Yuvarani Kasinathan Sivakami for support with a few experimental measurements.

References

1 G. J. Snyder and E. S. Toberer, Complex thermoelectric materials, *Nat. Mater.*, 2008, **7**, 105–114.
2 B. Poudel, Q. Hao, Y. Ma, Y. C. Lan, A. Minnich, B. Yu, X. Yan, D. Z. Wang, A. Muto, D. Vashaee, X. Y. Chen, J. M. Liu, M. S. Dresselhaus, G. Chen and Z. Ren, High-thermoelectric performance of nanostructured bismuth antimony telluride bulk alloys, *Science*, 2008, **320**, 634–638.
3 Y. Jiang, J. Dong, H.-L. Zhuang, J. Yu, B. Su, H. Li, J. Pei, F.-H. Sun, M. Zhou, H. Hu, J.-W. Li, Z. Han, B.-P. Zhang, T. Mori and J.-F. Li, Evolution of defect structures leading to high ZT in GeTe-based thermoelectric materials, *Nat. Commun.*, 2022, **13**, 6087.
4 J. Prado-Gonjal, E. García-Calvo, J. Gainza, O. J. Durá, C. Dejoie, N. M. Nemes, J. L. Martínez, J. A. Alonso and F. Serrano-Sánchez, Optimizing Thermoelectric Properties through Compositional Engineering in Ag-Deficient $AgSbTe_2$ Synthesized by Arc Melting, *ACS Appl. Electron. Mater.*, 2024, **6**, 2969–2977.
5 L. Li, B. Hu, Q. Liu, X.-L. Shi and Z.-G. Chen, High-Performance $AgSbTe_2$ Thermoelectrics: Advances, Challenges, and Perspectives, *Adv. Mater.*, 2024, **36**, e2409275.
6 D. Li, X.-L. Shi, Z. Feng, M. Li, J. Zhu, X. Ma, L. Zhang, H. Zhong, W.-D. Liu, S. Li and Z.-G. Chen, Fast Fabrication of High-Performance $CoSb_3$-Based Thermoelectric Skutterudites via One-Step Yb-Promoted Peritectic Solidification, *Adv. Funct. Mater.*, 2023, **33**(46), 2305269.
7 S. Zhang, S. Xu, H. Gao, Q. Lu, T. Lin, P. He and H. Geng, Characterization of multiple-filled skutterudites with high thermoelectric performance, *J. Alloys Compd.*, 2020, **814**, 152272.
8 K. Xia, C. Hu, C. Fu, X. Zhao and T. Zhu, Half-Heusler thermoelectric materials, *Appl. Phys. Lett.*, 2021, **118**(14), 140503.
9 R. J. Quinn and J.-W. G. Bos, Advances in half-Heusler alloys for thermoelectric power generation, *Mater. Adv.*, 2021, **2**, 6246–6266.
10 L. Xu, Y. Xiao, S. Wang, B. Cui, D. Wu, X. Ding and L.-D. Zhao, Dense dislocations enable high-performance PbSe thermoelectric at low-medium temperatures, *Nat. Commun.*, 2022, **13**, 6449.
11 I. T. Witting, T. C. Chasapis, F. Ricci, M. Peters, N. A. Heinz, G. Hautier and G. J. Snyder, The Thermoelectric Properties of Bismuth Telluride, *Adv. Electron. Mater.*, 2019, **5**, 1800904.
12 J. Pei, B. Cai, H.-L. Zhuang and J.-F. Li, Bi_2Te_3-based applied thermoelectric materials: research advances and new challenges, *Natl. Sci. Rev.*, 2020, **7**, 1856–1858.
13 J. Jiang, L. Chen, S. Bai, Q. Yao and Q. Wang, Thermoelectric properties of p-type $(Bi_2Te_3)_x(Sb_2Te_3)_{1-x}$ crystals prepared via zone melting, *J. Cryst. Grow.*, 2005, **277**, 258–263.
14 T. Wang, C. Zhou, W. Huang, X. Xia, H. Chen, Z. Li and J. Jiang, Synergistic Improvement of BiI3 and In on Thermoelectric Properties of Zone-Melted n-Type $Bi_2Te_{2.7}Se_{0.3}$, *ACS Appl. Mater. Interfaces*, 2024, **16**, 41080–41085.
15 H. C. Kim, T. S. Oh and D.-B. Hyun, Thermoelectric properties of the p-type Bi_2Te_3–Sb_2Te_3–Sb_2Se_3 alloys fabricated by mechanical alloying and hot pressing, *J. Phys. Chem. Solids*, 2000, **61**, 743–749.
16 S. K. Pundir, S. Singh and P. Jain, Spark Plasma Sintering Effect on Thermoelectric Properties of Nanostructured Bismuth Telluride Synthesized by High Energy Ball Milling, *J. Nanosci. Nanotechnol.*, 2020, **20**, 3902–3908.
17 J. H. Son, M. W. Oh, B. S. Kim, S. D. Park, B. K. Min, M. H. Kim and H. W. Lee, Effect of ball milling time on the thermoelectric properties of p-type $(Bi,Sb)_2Te_3$, *J. Alloys Compd.*, 2013, **566**, 168–174.
18 H. Li, H. Jing, Y. Han, G.-Q. Lu and L. Xu, Effects of mechanical alloying process and sintering methods on the microstructure and thermoelectric properties of bulk $Bi_{0.5}Sb_{1.5}Te_3$ alloy, *Intermetallics*, 2013, **43**, 16–23.
19 C.-H. Kuo, C.-S. Hwang, M.-S. Jeng, W.-S. Su, Y.-W. Chou and J.-R. Ku, Thermoelectric transport properties of

bismuth telluride bulk materials fabricated by ball milling and spark plasma sintering, *J. Alloys Compd.*, 2010, **496**, 687–690.

20 K. Hasezaki, T. Hamachiyo, M. Ashida, T. Ueda and Y. Noda, Thermoelectric Properties and Scattering Factors of Finely Grained Bi_2Te_3-Related Materials Prepared by Mechanical Alloying, *Mater. Trans.*, 2010, **51**, 863–867.

21 A. Kanatzia, C. Papageorgiou, C. Lioutas and T. Kyratsi, Design of Ball-Milling Experiments on Bi_2Te_3 Thermoelectric Material, *J. Electron. Mater.*, 2013, **42**, 1652–1660.

22 M. Kitamura, K. Hirota and K. Hasezaki, Relationships between Thermoelectric Properties and Milling Rotational Speed on $Bi_{0.3}Sb_{1.7}Te_{3.0}$ Thermoelectric Materials, *Mater. Trans.*, 2018, **59**, 1225–1232.

23 Z.-H. Ge, Y.-H. Ji, Y. Qiu, X. Chong, J. Feng and J. He, Enhanced thermoelectric properties of bismuth telluride bulk achieved by telluride-spilling during the spark plasma sintering process, *Scr. Mater.*, 2018, **143**, 90–93.

24 Z. Zhang, M. Sun, J. Liu, L. Cao, M. Su, Q. Liao, Y. Deng and L. Qin, Ultra-fast fabrication of Bi_2Te_3 based thermoelectric materials by flash-sintering at room temperature combining with spark plasma sintering, *Sci. Rep.*, 2022, **12**, 10045.

25 B. Chen, M. Kruse, B. Xu, R. Tutika, W. Zheng, M. D. Bartlett, Y. Wu and J. C. Claussen, Flexible thermoelectric generators with inkjet-printed bismuth telluride nanowires and liquid metal contacts, *Nanoscale*, 2019, **11**, 5222–5230.

26 B. Chen, S. R. Das, W. Zheng, B. Zhu, B. Xu, S. Hong, C. Sun, X. Wang, Y. Wu and J. C. Claussen, Inkjet Printing of Single-Crystalline Bi_2Te_3 Thermoelectric Nanowire Networks, *Adv. Electron. Mater.*, 2017, **3**, 1600524.

27 Z. Wang, W. Cui, H. Yuan, X. Kang, Z. Zheng, L. Chen, Q. Hu, W. Qiu, J. Tang and X. Cui, Direct ink writing of high-performance Bi_2Te_3-based thermoelectric materials using quasi-inorganic inks and interface engineering, *J. Mater. Chem. A*, 2022, **10**, 12921–12927.

28 A. Amin, R. Huang, D. Newbrook, V. Sethi, S. Yong, S. Beeby and I. Nandhakumar, Screen-printed bismuth telluride nanostructured composites for flexible thermoelectric applications, *J. Phys. Energy*, 2022, **4**, 24003.

29 Z. Cao, E. Koukharenko, M. J. Tudor, R. N. Torah and S. P. Beeby, Flexible screen-printed thermoelectric generator with enhanced processes and materials, *Sens. Actuators, A*, 2016, **238**, 196–206.

30 D. Madan, Z. Wang, A. Chen, R.-C. Juang, J. Keist, P. K. Wright and J. W. Evans, Enhanced performance of dispenser printed MA n-type Bi(2)Te(3) composite thermoelectric generators, *ACS Appl. Mater. Interfaces*, 2012, **4**, 6117–6124.

31 Y. S. Jung, D. H. Jeong, S. B. Kang, F. Kim, M. H. Jeong, K.-S. Lee, J. S. Son, J. M. Baik, J.-S. Kim and K. J. Choi, Wearable solar thermoelectric generator driven by unprecedentedly high temperature difference, *Nano Energy*, 2017, **40**, 663–672.

32 P. J. Yvon and R. B. Schwarz, Effects of iron impurities in mechanical alloying using steel media, *J. Mater. Res.*, 1993, **8**, 239–241.

33 *Handbook of Materials Failure Analysis with Case Studies from the Oil and Gas Industry*, ed. A. S. H. Makhlouf and M. Aliofkhazraei, Butterworth-Heinemann, Oxford, 2016.

34 J. Y. Yang, X. A. Fan, R. G. Chen, W. Zhu, S. Q. Bao and X. K. Duan, Consolidation and thermoelectric properties of n-type bismuth telluride-based materials by mechanical alloying and hot pressing, *J. Alloys Compd.*, 2006, **416**, 270–273.

35 T. Dasgupta and A. M. Umarji, Role of milling parameters and impurity on the thermoelectric properties of mechanically alloyed chromium silicide, *J. Alloys Compd.*, 2008, **461**, 292–297.

36 I. T. Witting, F. Ricci, T. C. Chasapis, G. Hautier and G. J. Snyder, The Thermoelectric Properties of n-Type Bismuth Telluride: Bismuth Selenide Alloys $Bi_2Te_{3-x}Se_x$, *Research*, 2020, **2020**, 4361703.

37 W. Wang, Y. Sun, Y. Feng, H. Qin, J. Zhu, F. Guo, W. Cai and J. Sui, High thermoelectric performance bismuth telluride prepared by cold pressing and annealing facilitating large scale application, *Mater. Today Phys.*, 2021, **21**, 100522.

38 R.-S. Zhai and T.-J. Zhu, Improved thermoelectric properties of zone-melted p-type bismuth-telluride-based alloys for power generation, *Rare Met.*, 2022, **41**, 1490–1495.

39 T. Parashchuk, O. Kostyuk, L. Nykyruy and Z. Dashevsky, High thermoelectric performance of p-type $Bi_{0.5}Sb_{1.5}Te_3$ films on flexible substrate, *Mater. Chem. Phys.*, 2020, **253**, 123427.

40 D. Ding, F. Sun, F. Xia and Z. Tang, A high-performance and flexible thermoelectric generator based on the solution-processed composites of reduced graphene oxide nanosheets and bismuth telluride nanoplates, *Nanoscale Adv.*, 2020, **2**, 3244–3251.

41 N. Su, P. Zhu, Y. Pan, F. Li and B. Li, 3D-printing of shape-controllable thermoelectric devices with enhanced output performance, *Energy*, 2020, **195**, 116892.

42 G.-P. Cui, C.-P. Feng, S.-C. Xu, K.-Y. Sun, J.-C. Ji, L. Hou, H.-B. Lan, H.-J. Shang and F.-Z. Ding, 3D-printed Bi_2Te_3-based Thermoelectric Generators for Energy Harvesting and Temperature Response, *ACS Appl. Mater. Interfaces*, 2024, **16**, 35353–35360.